



# Lab on a Chip

## Functional angiogenesis requires microenvironmental cues balancing endothelial cell migration and proliferation

Journal:	<i>Lab on a Chip</i>
Manuscript ID	LC-ART-11-2019-001170.R1
Article Type:	Paper
Date Submitted by the Author:	09-Feb-2020
Complete List of Authors:	Wang, William; University of Michigan Department of Biomedical Engineering, Biomedical Engineering Lin, Daphne; University of Michigan, Biomedical Engineering Jarman, Evan; University of Michigan, Biomedical Engineering Polacheck, William; University of North Carolina at Chapel Hill, Biomedical Engineering Baker, Brendon; University of Michigan, Biomedical Engineering

SCHOLARONE™  
Manuscripts

1 **Functional angiogenesis requires microenvironmental cues balancing endothelial cell migration and**  
2 **proliferation**

3 William Y. Wang<sup>1</sup>, Daphne Lin<sup>1</sup>, Evan H. Jarman<sup>1</sup>, William J. Polacheck<sup>2</sup>, Brendon M. Baker<sup>1,+</sup>

4

5 <sup>1</sup>Department of Biomedical Engineering

6 University of Michigan

7 Ann Arbor, MI 48109

8 <sup>2</sup>Joint Department of Biomedical Engineering

9 University of North Carolina at Chapel Hill and North Carolina State University

10 Chapel Hill, NC 27514

11

12 <sup>+</sup> Corresponding Author:

13 Brendon M. Baker, Ph.D.

14 Department of Biomedical Engineering, University of Michigan

15 2174 Lurie BME Building, 1101 Beal Avenue

16 Ann Arbor, MI 48109

17 Email: bambren@umich.edu

18

19 Key words: Angiogenesis, Cell Migration, Cell Proliferation, Microfluidics, Extracellular Matrix,

20 Microenvironment, Endothelial Cells, Chemotaxis, Hydrogels, Microvasculature, Sprouting Morphogenesis

21 **ABSTRACT**

22           Angiogenesis is a complex morphogenetic process that involves intimate interactions between  
23 multicellular endothelial structures and their extracellular milieu. *In vitro* models of angiogenesis can aid in  
24 reducing the complexity of the *in vivo* microenvironment and provide mechanistic insight into how soluble and  
25 physical extracellular matrix cues regulate this process. To investigate how microenvironmental cues regulate  
26 angiogenesis and the function of resulting microvasculature, we multiplexed an established angiogenesis-on-a-  
27 chip platform that affords higher throughput investigation of 3D endothelial cell sprouting emanating from a  
28 parent vessel through defined biochemical gradients and extracellular matrix. We found that two fundamental  
29 endothelial cell functions, migration and proliferation, dictate endothelial cell invasion as single cells vs.  
30 multicellular sprouts. Microenvironmental cues that elicit excessive migration speed incommensurate with  
31 proliferation resulted in microvasculature with poor barrier function and an inability to transport fluid across  
32 the microvascular bed. Restoring the balance between migration speed and proliferation rate rescued  
33 multicellular sprout invasion, providing a new framework for the design of pro-angiogenic biomaterials that  
34 guide functional microvasculature formation for regenerative therapies.

## 35 **INTRODUCTION**

36           The microvascular network of arterioles, capillaries, and venules is a critical component of the circulatory  
37 system required for the function and maintenance of nearly every tissue in the human body. Once regarded  
38 simply as passive fluidic microstructures, it is now understood that the microvasculature (vessels <50  $\mu\text{m}$  in  
39 diameter) dynamically alters its structure and function to service the changing metabolic demands of tissues<sup>1,2</sup>.  
40 Rapid changes in microvessel diameter through vasoconstriction or vasodilation allow for temperature and  
41 blood pressure regulation<sup>3</sup>. In response to tissue injury, local microvasculature rapidly adjusts permeability,  
42 enabling immune cells to extravasate and fight infection; over longer timescales, the microvasculature expands  
43 to revascularize the healing tissue<sup>4</sup>. Angiogenesis, the formation of new microvasculature from an existing  
44 parent vessel, is the predominant method by which microvasculature extends and is critical to tissue healing  
45 and homeostasis<sup>5</sup>. Indeed, dysregulated angiogenesis producing excessive or insufficient microvasculature is a  
46 hallmark of many diseases, and as such, microvascular morphology and function are clinical indicators of  
47 pathology<sup>6,7</sup>. During cancer progression for example, abnormal gradients of soluble pro-angiogenic factors  
48 recruit endothelial cells (ECs) from adjacent tissues to invade into the tumor stroma<sup>8</sup>. This rapid and excessive  
49 angiogenesis results in a high density of disorganized and highly permeable neovessels that facilitates tumor  
50 growth and provides metastatic access<sup>9</sup>. In contrast, insufficient angiogenesis impairs tissue regeneration for  
51 example in cardiac ischemia or diabetic foot ulcers<sup>10</sup>. An understanding of how the surrounding  
52 microenvironment appropriately guides the formation of functional microvasculature rather than excessive or  
53 insufficient angiogenesis in disease contexts would be critical to designing vascularized biomaterials for  
54 regenerative medicine and novel therapies to treat vasculopathies<sup>6,11,12</sup>.

55           Observations consistent across a wide range of *in vivo* and *in vitro* models of angiogenesis have  
56 established several key steps including (1) chemokine gradients promoting endothelial tip cell formation and  
57 directed invasion into the extracellular matrix (ECM), (2) collective migration of leading tip cells and ensuing  
58 stalk cells, (3) proliferation and lumenization of the invading strand, and (4) maturation into functional

59 neovasculature<sup>13,14</sup>. Each of these steps is regulated by both biochemical and physical microenvironmental cues  
60 presented by the surrounding ECM, the 3D fibrous, collagenous meshwork through which EC sprouts navigate<sup>15</sup>.  
61 As characterizing and tuning microenvironmental cues (e.g. profiling biochemical gradients and controlling  
62 physical ECM properties) is challenging *in vivo*, *in vitro* models have proven instrumental in providing  
63 mechanistic insight into each step of angiogenesis<sup>16</sup>. To build our understanding of how ECs migrate collectively,  
64 2D scratch wound assays are widely utilized. While these assays have provided detailed insight into the  
65 molecular pathways governing collective migration of EC monolayers<sup>17</sup>, the model fails to recapitulate the 3D  
66 nature of sprouting morphogenesis<sup>18</sup>. EC outgrowth assays from spheroids or microbead carriers embedded  
67 within 3D ECM have been instrumental in studying the role of matrix proteolysis and tip vs. stalk cell identity  
68 and dynamics<sup>19–23</sup>. However, sprouts in these models do not originate from an accessible lumenized parent  
69 vessel, making it difficult to assess key microvascular functions such as fluidic connectivity and permeability.  
70 More recently, advances in biomicrofluidics and efforts to engineer tissues-on-chips have generated 3D human  
71 engineered microvessels<sup>24–26</sup>; these models have been utilized to study how chemokine gradients, ECM  
72 degradability, shear stress and support cells regulate vessel barrier function, EC sprouting and tumor and  
73 immune cell extravasation<sup>24,25,27–29</sup>. While much information has been learned from these various models, how  
74 EC migration speed and proliferation – two fundamental cell processes required for angiogenesis – influence  
75 the formation and function of subsequent microvasculature remains unresolved.

76 In this work, we multiplexed a microfluidic device that recapitulates key aspects of sprouting  
77 morphogenesis, namely the directional, chemokine-driven invasion of ECs from the stable and quiescent  
78 endothelium of a fluid-bearing arteriole-scale parent vessel into the surrounding 3D ECM. We used this  
79 biomimetic model to investigate how soluble and physical ECM properties regulates EC invasion speed and  
80 proliferation during sprouting and how independently tuning the rate of these two basic cell functions influences  
81 the quality of formed microvasculature. We find that the formation of functional microvasculature capable of  
82 transporting fluid and performing barrier function requires a delicate balance between EC migration speed and

83 proliferation rate. Furthermore, we demonstrate that aberrant angiogenic sprouting driven by altered physical  
84 and soluble microenvironmental cues can in fact be rescued by correcting the imbalance between these two  
85 fundamental EC functions. As the proper vascularization of large tissue engineered constructs remains an  
86 outstanding challenge for the biomedical engineering community, the findings of this work establish a new  
87 framework for biomaterial design parameters that balance EC migration speed and proliferation to optimally  
88 generate functional microvasculature.

89 **RESULTS**90 **Multiplexed angiogenesis-on-a-chip platform**

91 To investigate how soluble and physical microenvironmental cues regulate angiogenic sprouting, we  
92 adapted a previously established microfluidic device that recapitulates 3D EC sprouting morphogenesis from  
93 the stable, quiescent endothelium of a parent vessel<sup>28,29</sup>. The parent vessels modeled in this work possess a  
94 diameter that lies near the upper end of values previously described for arterioles, but lack additional support  
95 cells such as vascular smooth muscle cells and pericytes<sup>30,31</sup>. We improved the fabrication throughput of these  
96 devices by reducing their assembly to a single layer design in addition to multiplexing the number of devices  
97 resulting from each fabrication such that a single chip contains a 2x4 array of devices (Fig. 1a). To generate  
98 parent vessels in these devices, a hydrogel precursor solution is first injected through device ports and is allowed  
99 to crosslink around two parallel needles (300  $\mu\text{m}$  diameter) suspended across each device's central chamber  
100 (Fig. 1a-b). The void space created after needle extraction forms a pair of parallel hollow channels fully  
101 embedded within extracellular matrix (ECM) terminating in two media reservoirs (Fig. 1b). ECs seeded into one  
102 channel of each device attach to the inner channel surface and self-assemble into a perfused endothelialized  
103 tube serving as the parent vessel (300  $\mu\text{m}$  diameter, 3 mm length, Fig. 1c-e). Within 24 hours, the assembled EC  
104 monolayer of the engineered parent vessel localizes VE-cadherin to cell-cell junctions and maintains a consistent  
105 diameter and cell density over a range of collagen densities (Fig. 1d and Supplemental Fig. 1a-d).

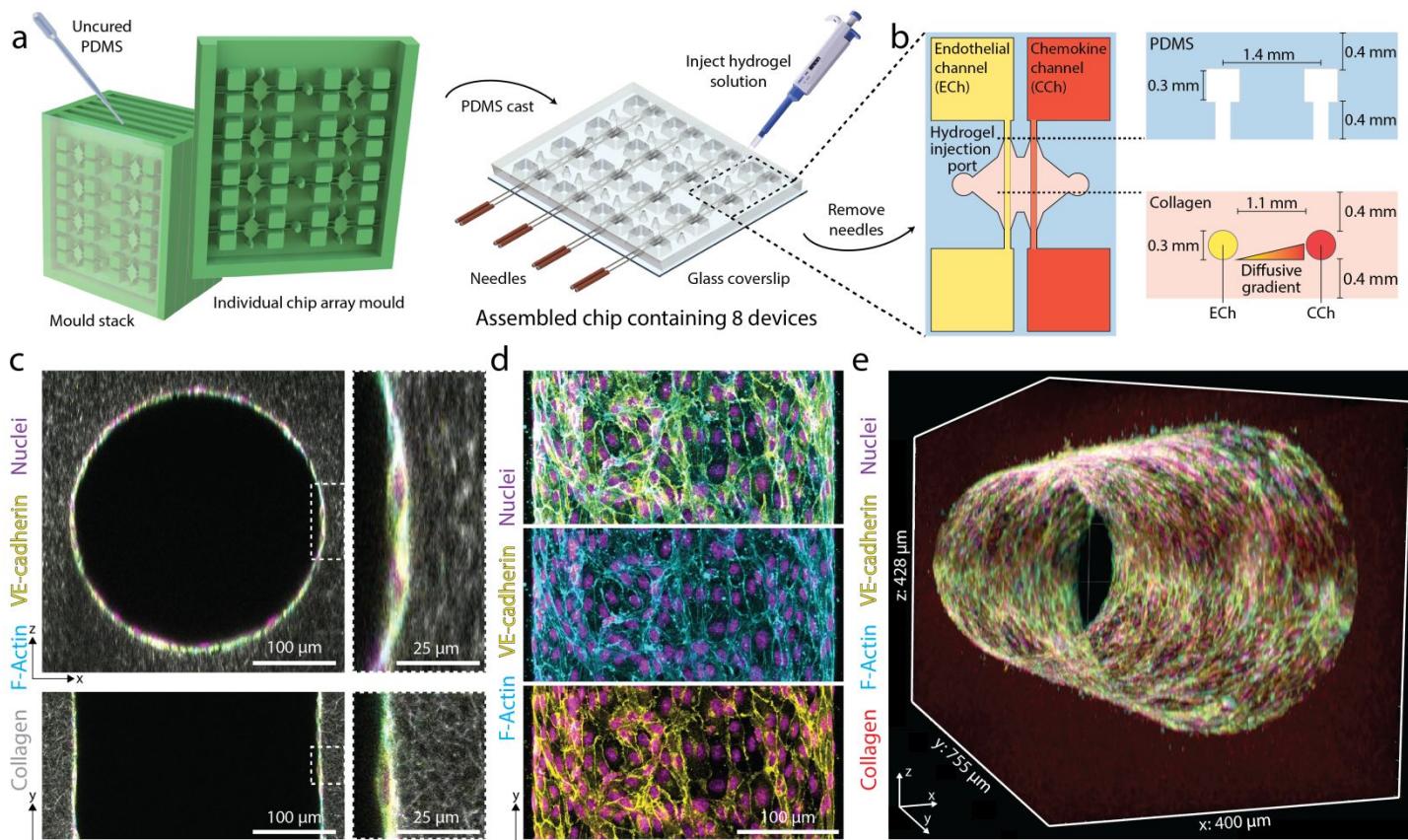


**Figure 1 | Multiplexed angiogenesis-on-a-chip platform.** **a**, PDMS replica casts from 3D-printed moulds are bonded to glass coverslips. Each chip is composed of a 2x4 array of single devices. A pair of needles are inserted into each device, and type I collagen solution is injected into each device and gelled around needles. Hollow channels are generated upon needle removal. **b**, Inserted needles are suspended above the glass coverslip bottom and below the PDMS housing to form 3D channels fully embedded within a collagen hydrogel. Each device is composed of two parallel channels. The endothelial channel (ECh) is seeded with endothelial cells to form the parent vessel. Pro-angiogenic factors are added to the chemokine channel (CCh) and form a diffusive gradient to promote 3D endothelial cell invasion across the collagen hydrogel. **c**, Representative images of x-z (top) and x-y (bottom) orthogonal views of parent vessels formed within fluorescently labeled 3 mg ml<sup>-1</sup> collagen hydrogel 24-hours post-seeding. Insets indicated with dashed white lines. **d**, Representative images of x-y (max intensity projection) formed within a 3 mg ml<sup>-1</sup> collagen hydrogel 24-hours post-seeding. Merge (top), F-actin (middle), VE-cadherin (bottom). **e**, 3D rendering of parent vessel formed within fluorescently labeled 3mg ml<sup>-1</sup> collagen hydrogel.

### Soluble factors regulate multicellular sprouting

Utilizing 3 mg ml<sup>-1</sup> collagen, parent vessels cultured in EGM2 proved stable as single ECs minimally invaded ( $5.5 \pm 14.9 \mu\text{m}$ ) into the ECM over 5-day culture under continual reciprocating flow (Fig. 2a, c). To induce EC invasion, we introduced an established EC chemoattractant, sphingosine 1-phosphate (S1P), to the adjacent chemokine channel to produce a diffusive gradient that drives directional 3D EC invasion through the ECM<sup>28,29,32</sup>. We found EC invasion depth over 5-day culture to be dependent on [S1P], with increasing [S1P] resulting in increased invasion speed (Fig. 2a, c). To assess the morphologic quality of EC invasion, we categorized ECs as isolated single cells or multicellular sprouts and determined the ratio of sprouts to single cells as a metric of

127 invasion multicellularity. Due to variations in invasion depth across conditions, we restricted quantification of  
128 single cells to 150  $\mu\text{m}$  from the leading invasive front and defined sprouts as contiguous multicellular structures  
129 with a length greater than half the max invasion depth (Supplemental Fig. 2). Although [S1P] clearly mediated  
130 cell invasion in a dose-dependent manner, the phenotype of invading ECs was primarily as single, disconnected  
131 cells and multicellular sprouts were rarely observed (Fig. 2a, c, e-g). Due to the low levels of EC proliferation  
132 observed in these conditions (Fig. 2d) and given previous evidence that EC proliferation is required for  
133 angiogenesis *in vivo*<sup>33,34</sup>, we hypothesized that enhancing proliferation rates would increase the number of ECs  
134 collectively invading as multicellular sprouts. Media supplementation with 25  $\text{ng ml}^{-1}$  phorbol 12-myristate 13-  
135 acetate (PMA), another well-established pro-angiogenic factor and potent activator of PKC<sup>28,29,35,36</sup>, resulted in  
136 elevated proliferation rates as assayed by EdU incorporation (Fig. 2d). Few invading ECs were observed at 0 nM  
137 S1P with 25  $\text{ng ml}^{-1}$  PMA implying that the addition of PMA alone does not induce EC invasion (Fig. 2b-c).  
138 Invasion speed remained S1P dose-dependent in the presence of 25  $\text{ng ml}^{-1}$  PMA while proliferation rates  
139 proved independent of S1P dose (Fig. 2b-d). In support of our hypothesis, PMA supplementation and elevated  
140 EC proliferation corresponded to significant increases in the number of invading multicellular sprouts at each  
141 level of [S1P] (Fig. 2d-g, Supplemental Fig. 3, Supplemental Movie 1-3). In conditions with 25  $\text{ng ml}^{-1}$  PMA, sprout  
142 invasion depth over 5-day culture anti-correlated with the ratio of multicellular sprouts to single ECs (Fig. 2c, g);  
143 the highest level of S1P (500 nM) resulting in the fastest invasion speed, most single cells, and fewest  
144 multicellular sprouts (Fig. 2c, e-f). These data clearly indicate proliferation in this model is a requirement for  
145 multicellular sprout invasion, supporting previous observations *in vivo*<sup>33,34</sup>. Furthermore, while a chemokine  
146 gradient is an additional key requirement for angiogenesis, stronger gradients that increase invasion speed elicit  
147 a single cell migration phenotype in lieu of multicellular sprouts.

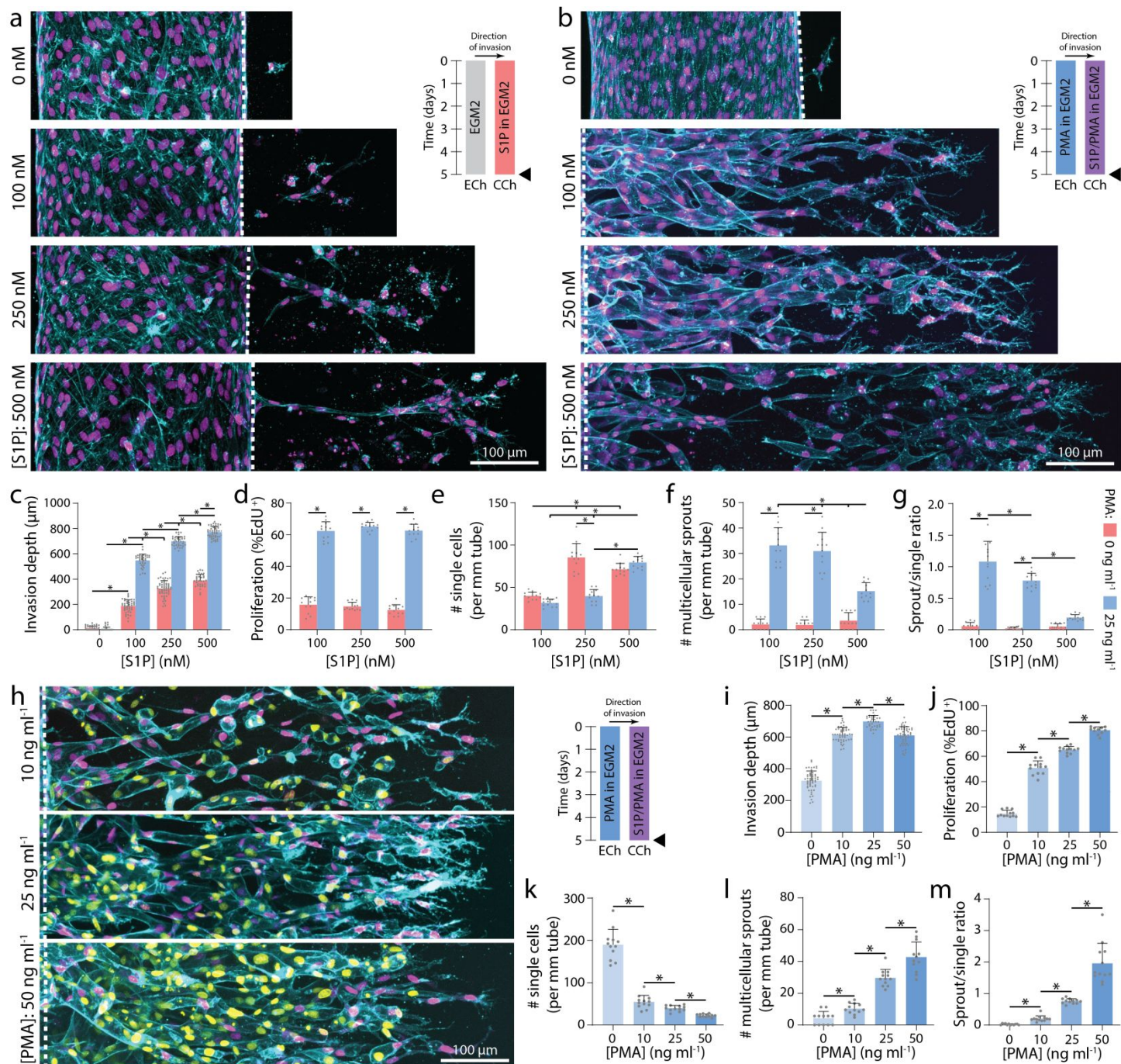
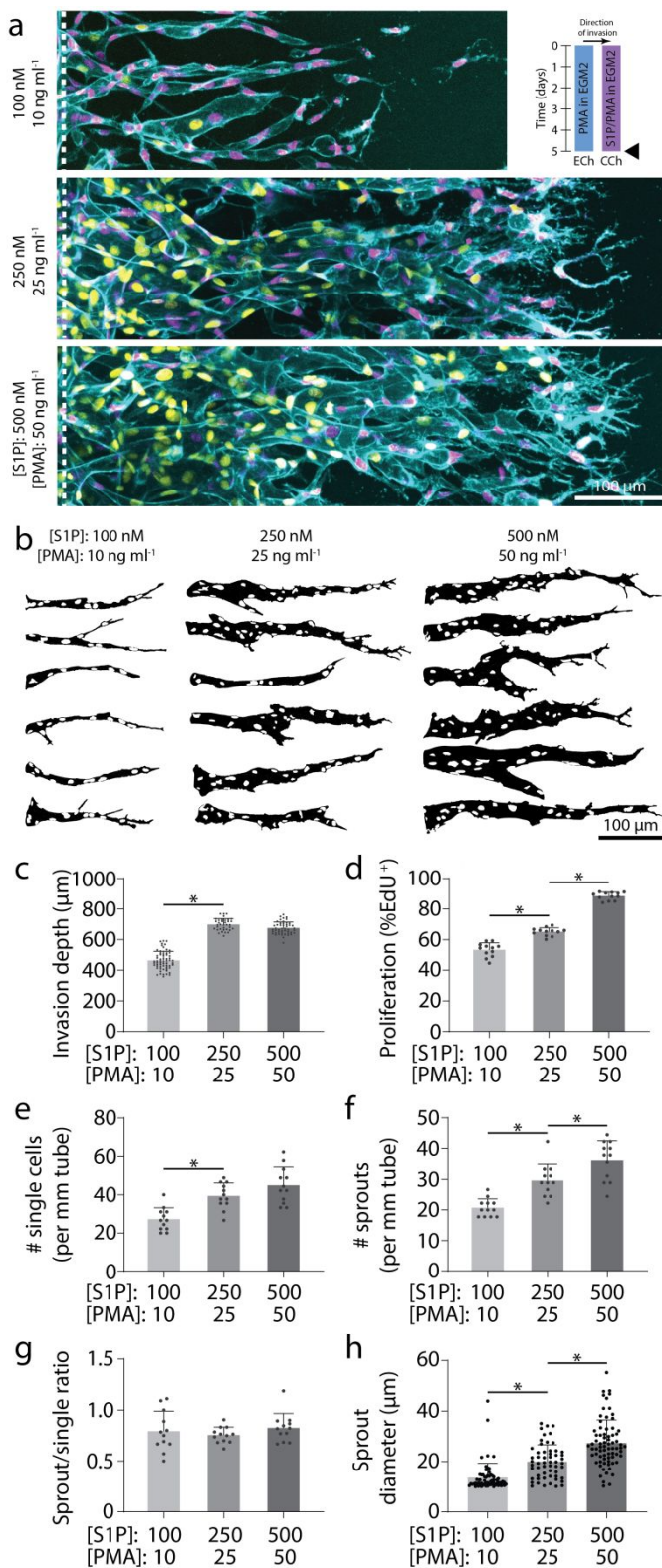


**Figure 2 | Soluble factors modulate EC invasion, proliferation, and multicellular sprouting.** **a**, Representative images (max intensity projection) of invading endothelial cells in response to varying [S1P]. **b**, Representative images (max intensity projection) of invading endothelial cells in response to varying [S1P] with 25 ng ml<sup>-1</sup> PMA. F-actin (cyan), nucleus (magenta), and dashed white lines indicate parent vessel edge (**a-b**). **c-g**, Quantifications of invasion depth, proliferation, and morphology of invading endothelial cells as single cells or multicellular sprouts. **h**, Representative images (max intensity projection) of invading endothelial cells in response to varying [PMA] with 250 nM S1P. **i-m**, Quantifications of invasion depth, proliferation, and morphology of invading endothelial cells as single cells or multicellular sprouts. UEA (cyan), nucleus (magenta), EdU (yellow). All data presented as mean  $\pm$  s.d.; \* indicates a statically significant comparison with  $P < 0.05$  (one-way analysis of variance). For invasion depth analysis (**c**, **i**),  $n \geq 32$  vessel segments (each 100  $\mu\text{m}$  length) per condition; for proliferation and migration mode analysis (**d-g**, **j-m**),  $n = 12$  vessel segments (each 800  $\mu\text{m}$  length) per condition from  $n = 2$  devices/condition (technical replicates) over  $n \geq 4$  independent studies (biological replicates).

160 To investigate the effects of proliferation rates on multicellular angiogenic sprouting, we next varied  
161 [PMA] while maintaining [S1P] constant at 250 nM. Proliferation rates proved PMA dose-dependent and  
162 positively correlated with the number of multicellular sprouts (Fig. 2h, j-m, Supplemental Fig. 3, Supplemental  
163 Movie 4-5). Although PMA alone did not induce EC invasion (Fig. 2b-c), increasing [PMA] in the presence of S1P  
164 resulted in a biphasic relationship with invasion depth (Fig. 2i). The influence of increasing [PMA] from 0 to 25  
165 ng ml<sup>-1</sup> on increased invasion depth may be due to a greater number of invading cells each secreting matrix  
166 metalloproteinases (MMPs). Elevated MMP levels would hasten localized matrix degradation, allowing ECs to  
167 more rapidly generate open space within 3D ECM required to advance forward. Interestingly, at the highest  
168 tested concentration of PMA resulting in the most proliferation, invasion depth decreased (Fig. 2i). As cells are  
169 transiently non-migratory during mitosis, this decrease may stem from frequent proliferative events hampering  
170 efficient migration of ECs. Varying [PMA] and thus PKC activation may have multiple downstream effects, so we  
171 treated ECs with mitomycin C (a crosslinker that prevents DNA replication and inhibits mitosis) to confirm the  
172 role of proliferation as the primary effector of enhancing multicellular sprout invasion. Even in the presence of  
173 the highest level of PMA, proliferation-inhibited ECs invaded only as single cells with significantly decreased  
174 invasion depth as compared to controls (Supplemental Fig. 4a-f). These studies therefore indicate cell  
175 proliferation is not only required for multicellular sprout invasion, but additionally influences the rate at which  
176 sprouts traverse 3D ECM.

177 In the experiments above individually modulating migration speed and proliferation, higher migration  
178 speeds resulted in disconnected single EC invasion while increasing proliferation rates enhanced multicellular  
179 sprouting. We thus hypothesized that proliferation rate commensurate with invasion speed is essential to the  
180 collective invasion of multicellular sprouts. Indeed, proportionally increasing or decreasing both [S1P] and [PMA]  
181 simultaneously resulted in invasion depth and proliferation rate increases or decreases, respectively, but did  
182 not alter the ratio of multicellular sprouts to single ECs (Fig. 3a-g). This suggests that multicellular angiogenic  
183 sprouting requires a critical balance between EC invasion speeds and proliferation rates, which can be finely

184 tuned by these two established soluble pro-angiogenic factors. While balanced soluble conditions maintained  
185 similar invasion multicellularity, the magnitude of these cues influenced sprout diameter, with higher levels of  
186 S1P and PMA increasing sprout diameter (Fig. 3a-b, h). Larger neovessel diameters would allow for increased  
187 fluid transport, but smaller diameter vessels would allow for increased capillary density and more efficient  
188 nutrient-waste exchange. Although this requires further exploration, including investigation of the influence of  
189 vascular smooth muscle cells and pericytes that support microvasculature *in vivo*<sup>37,38</sup>, here we demonstrate that  
190 tuning concentrations of soluble factors regulates EC sprout diameters within the diameter range of  
191 microvasculature (<50  $\mu\text{m}$ )<sup>2,30,31</sup>.



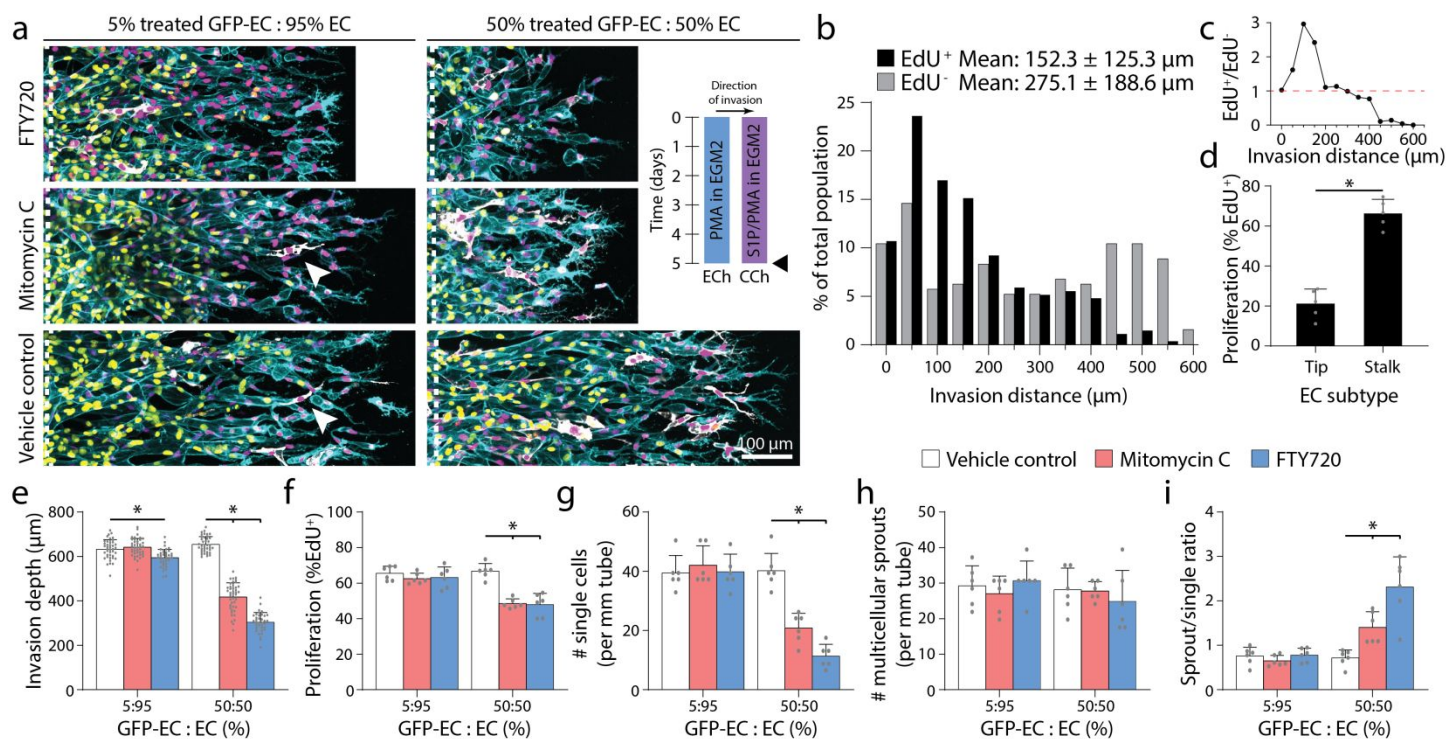
192 **Figure 3 | Multicellular sprouting requires balanced migration and proliferation.** **a**, Representative images (max intensity projection)  
 193 of invading endothelial cells in response to proportional variations of [S1P] and [PMA]. UEA (cyan), nucleus (magenta), EdU (yellow).  
 194 **b**, Representative sprout outlines from conditions in **(a)**. **c-h**, Quantifications of invasion depth, proliferation, morphology of invading  
 195 endothelial cells as single cells or multicellular sprouts, and sprout diameter. All data presented as mean ± s.d.; \* indicates a statically  
 196 significant comparison with P<0.05 (one-way analysis of variance). For invasion depth analysis **(c)**, n≥36 vessel segments (each 100 μm  
 197 length) per condition. For proliferation and migration mode analysis **(d-g)**, n=12 vessel segments (each 800 μm length) per condition  
 198 from n=2 devices/condition (technical replicates) over n≥4 independent studies (biological replicates). For sprout diameter analysis  
 199 **(h)**, n≥56 sprout segments.  
 200

**201 Differential roles of tip and stalk endothelial cells**

202 Previous work indicates that tip cells responsive to angiogenic chemokine gradients lead invading  
203 sprouts by degrading the ECM and guiding ensuing stalk cells<sup>13,14</sup>. To investigate whether tip cells require  
204 chemokine receptors, we performed mosaic sprouting studies where untreated ECs were mixed with GFP-  
205 labeled ECs pre-treated with FTY720 (FTY720-GFP-ECs), an S1P receptor inhibitor. Preliminary studies confirmed  
206 the inhibitory effect of FTY720, as ECs pre-treated with 100 nM FTY720 prior to device seeding demonstrated  
207 minimal invasion over 5-day culture despite appropriate soluble conditions of 250 nM S1P and 25 ng ml<sup>-1</sup> PMA  
208 (S250:P25) (Supplemental Fig. 5a-b). Furthermore, when ECs were allowed to sprout for 3 days prior to FTY720  
209 treatment, subsequent S1P receptor inhibition halted any further advance of already established sprouts  
210 (Supplemental Fig. 5a-b). Performing mosaic studies with controlled ratios of FTY720-GFP-ECs vs. untreated ECs,  
211 a higher fraction of FTY720-GFP-ECs decreased invasion depth, the number of single ECs, and thereby enhanced  
212 sprout multicellularity as evident by increased sprout-single cell ratios (Fig. 4a, e-i). Furthermore, FTY720-GFP-  
213 ECs primarily remained in the parent vessel and did not assume the tip cell position of invading sprouts. FTY720-  
214 GFP-ECs were occasionally found within sprout stalks, suggesting that pushing or pulling forces from adjacent  
215 stalk cells may enable the movement of FTY-GFP-ECs lacking functional S1P receptors.

216 Previous work *in vivo* has shown that the frequency of proliferation is spatially segregated by EC subtype  
217 (i.e. tip and stalk ECs)<sup>19,34</sup>. Examining the localization of proliferation during sprouting angiogenesis in this model,  
218 ECs at the invasion front were indeed the least proliferative (Fig. 4b-c). Furthermore, while only a small  
219 percentage of tip ECs underwent proliferation, the majority of EdU<sup>+</sup> nuclei were positioned within sprout stalks  
220 closest to the parent channel (Fig. 4b-d). To test whether tip cells require proliferative capacity, we performed  
221 additional mosaic studies seeding parent vessels with mixtures of mitomycin C pre-treated GFP-labeled ECs  
222 (MitoC-GFP-EC) and untreated ECs. At low mosaic ratios (5% MitoC-GFP-EC) where overall sprouting was not  
223 influenced by non-proliferating ECs, MitoC-GFP-ECs were observed at the tip cell position, confirming previous  
224 observations *in vivo* that tip cells do not require the capacity to proliferate (Fig. 4a, e-i)<sup>19,34</sup>. At high mosaic ratios

225 (50% MitoC-GFP-EC), overall proliferation rates decreased as expected (Fig. 4f). While impaired proliferation  
 226 should decrease multicellular sprouting based on the studies above (Fig. 2h-m), invasion speeds also decreased  
 227 such that the balance between migration speed and proliferation was maintained and the number of  
 228 multicellular sprouts did not differ from controls (Fig. 4e-f, h). With decreased invasion speed, fewer tip cells at  
 229 the invasive front broke away as single cells resulting in enhanced ratios of sprouts to single cells (Fig. 4g-i).  
 230 Taken together, tip and stalk cells perform differential roles during sprouting and possess distinct requirements  
 231 for chemotaxis and proliferation. Tip cells require chemokine receptors to migrate in response to soluble  
 232 gradients, but do not require proliferative capacity; in contrast, proliferation primarily occurs in ensuing stalk  
 233 cells, perhaps providing a requisite cell density needed to maintain intercellular connectivity within the invading  
 234 multicellular structure.



235 **Figure 4 | Invading tip cells require chemokine receptors but do not require proliferative capacity.** **a**, Representative images (max  
 236 intensity projection) of invading endothelial cells with S250:P25 and varying ratios of treated GFP-EC to untreated EC with indicated  
 237 treatment. UEA (cyan), nucleus (magenta), EdU (yellow), GFP-EC (white). **b**, Histogram of EdU<sup>+</sup> and EdU<sup>-</sup> invaded endothelial cells with  
 238 S250-P25 after 5-day culture. **c**, Ratio of EdU<sup>+</sup> to EdU<sup>-</sup> endothelial cells from **(b)**. **d**, Percentage of EdU<sup>+</sup> tip or stalk cells from **(b)**. **e-i**,  
 239 Quantifications of invasion depth, proliferation, and morphology of invading endothelial cells as single cells or multicellular sprouts.  
 240 All data presented as mean ± s.d.; \*indicates a statically significant comparison with P<0.05 (two-tailed Student's t-test **(d)** and one-  
 241 way analysis of variance **(e-i)**). For spatial EdU analysis **(b-c)**, n≥192 cells. For tip vs. stalk proliferation analysis **(d)**, n= 5 vessel segments  
 242 (each 800 μm length). For invasion depth analysis **(e)**, n≥37 vessel segments (each 100 μm length) per condition. For proliferation and  
 243

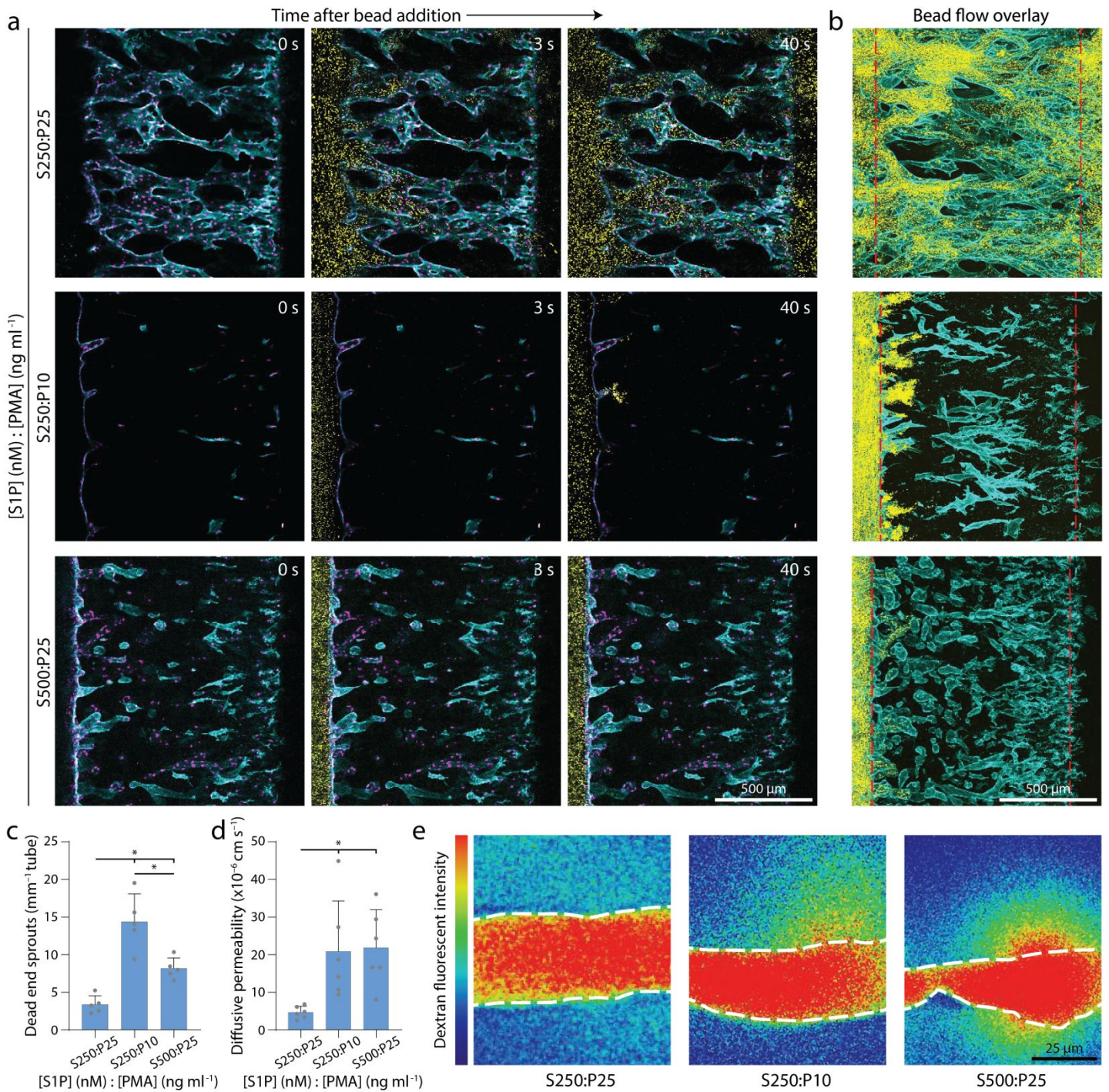
244 migration mode analysis (f-i), n=6 vessel segments (each 800  $\mu\text{m}$  length) per condition from n=2 devices/condition (technical  
245 replicates) over n $\geq$ 3 independent studies (biological replicates).

#### 246 **Functional assessment of fluidic connectivity and permeability**

247 A critical function of microvasculature is the transport of nutrients, waste, platelets, and immune cells.  
248 To assess the patency and fluidic connectivity of neovessels, we allowed ECs to fully traverse the 1.1 mm wide  
249 collagen matrix and reach the adjacent CCh. Time-lapse confocal imaging while introducing fluorescent  
250 microspheres ( $\emptyset = 1 \mu\text{m}$ ) into ECh reservoirs enabled rapid assessment of flow across the formed vascular bed  
251 (ECs spanning ECM). In vascular beds generated under balanced levels of invasion speed and proliferation rates  
252 (i.e. conditions resulting in high sprout-single ratios), beads readily flowed through the neovessel network  
253 spanning across ECh to CCh demonstrating fluidic connectivity of functional microvasculature (Fig. 5a). In stark  
254 contrast, dysfunctional microvascular beds formed with excessively high invasion speed (S500:P25) or deficient  
255 proliferation (S250:P10) resulting in disconnected sprouts (i.e. low sprout-single ratio), fluorescent  
256 microspheres failed to flow across the ECM space and remained sequestered near the endothelialized parent  
257 channel (Fig. 5a). Indeed, max intensity projections of the full height of the 3D vascularized ECM revealed a  
258 complete absence of bead flow, confirming observations from individual z-slices captured during time-lapse  
259 imaging (Fig. 5b).

260 Barrier function and endothelial permeability regulated by cell-cell junctions are a closely related aspect  
261 of microvascular function<sup>25</sup>. To assess the permeability of formed vascular beds, we introduced fluorescent 70  
262 kDa dextran to the endothelial parent channel after ECs fully traversed the collagen matrix reaching the adjacent  
263 CCh, allowed flow across the vascular bed, and time-lapse imaged dextran diffusion across neovessel walls into  
264 the surrounding ECM. Low permeability was only achieved when vascular beds were formed under soluble cues  
265 that balanced invasion speed with proliferation rates (Fig. 5d-e), and are comparable to reported values *in vivo*  
266 of protein diffusion across capillaries ( $4.3 \times 10^{-6} \text{ cm s}^{-1}$ )<sup>39</sup>. Interestingly, in both bead flow and permeability  
267 assessments, imbalanced soluble conditions resulting in disconnected sprouts were composed of neovessels  
268 that were highly permeable at the tip cell position, such that 1.0  $\mu\text{m}$  beads collected in the adjacent ECM (Fig.

269 5c). Taken together, multicellular invasion driven by soluble cues that balance invasion and proliferation yields  
 270 fluidically functional microvascular beds with low permeability. Beyond these two features critical for transport,  
 271 future efforts are required to assess other key functions of the microvasculature including gas exchange,  
 272 regulation of permeability in response to inflammatory cytokines, and the ability to initiate the clotting cascade  
 273 upon disruption of the endothelium.



275 **Figure 5 | Balanced migration and proliferation optimize microvasculature fluidic connectivity and permeability.** **a**, Representative  
276 time course images of 1  $\mu\text{m}$  bead flow across vascular beds formed with balanced cues (top), low proliferation (middle), and high  
277 migration (bottom). Nucleus (magenta), F-actin (cyan), beads (yellow). **b**, Max intensity projection at steady state from (**a**); red dashed  
278 lines indicate ECh and CCh edges. F-actin (cyan), beads (yellow). **c**, Quantification of sprouts incapable of fluidically transporting beads.  
279 **d**, Quantification of diffusive permeability of 70-kDa dextran. **e**, Representative heat map images of 70 kDa dextran diffusion across  
280 neovessels within vascular beds formed with balanced cues (left), low proliferation (center), and high migration (right). White dashed  
281 lines indicate vessel edge. All data presented as mean  $\pm$  s.d.; \* indicates a statically significant comparison with  $P < 0.05$  (one-way  
282 analysis of variance).  $n = 5$  devices per condition (**c**),  $n = 6$  neovessels per condition (**d**).  
283 **Matrix density regulates sprouting speed and morphology**

284 In addition to soluble cues, physical properties of the ECM are known to regulate EC morphology and  
285 function during angiogenesis<sup>15</sup>. We hypothesized that independent of soluble cues, physical ECM cues may also  
286 influence the balance between EC migration speed and proliferation, and therefore invasion as multicellular  
287 sprouts. For example, ECM density, stiffness, and degradability define the susceptibility of ECM to proteolytic  
288 activity required for 3D migration<sup>21,29,40</sup>. To investigate whether physical properties of ECM influence EC invasion  
289 as multicellular sprouts we tuned ECM density by modulating collagen concentration (all previous studies were  
290 performed in 3 mg ml<sup>-1</sup> collagen). Maintaining constant soluble cues of S250:P25, increasing collagen density  
291 resulted in decreased invasion depth over 3-day culture (Fig. 6a, d). Interestingly, varying collagen density from  
292 2-6 mg ml<sup>-1</sup> did not significantly alter EC proliferation rates, perhaps due to PMA's potent enhancement of  
293 proliferation (Fig. 6e). Mimicking the response of EC invasion speed to [S1P] (Fig. 2c), decreasing matrix density  
294 increased EC invasion speeds with a parallel shift in the morphology of invading ECs from primarily multicellular  
295 sprouts towards single cells (Fig. 6d, f-h). Time-lapse imaging capturing the dynamics of EC invasion revealed  
296 that tip ECs break away from the parent vessel more frequently in matrices with low collagen density (Fig. 6b-  
297 c). Furthermore, within multicellular sprouts, tip cells were also observed to lose connectivity with trailing stalk  
298 cells (Supplemental Fig. 6).

299 We thus hypothesized that reducing EC invasion speed in low density collagen would rescue multicellular  
300 sprout invasion by allowing trailing stalk cells to maintain intercellular connectivity with leading tip cells. We  
301 first decreased EC invasion speed by reducing the strength of the chemokine gradient. Decreasing [S1P] from  
302 250 nM to 100 nM resulted in decreased invasion speed and increased EC invasion as multicellular sprouts (Fig.

303 6i-m). To reduce 3D migration speed without modifying the chemokine gradient, we treated ECs with low doses  
304 of Marimastat (1 mM) to reduce MMP activity. In similar fashion to decreased [S1P], Marimastat treatment  
305 decreased invasion speed and increased EC invasion as multicellular sprouts (Fig. 6i-m). Taken together, an  
306 interplay of soluble and physical microenvironmental cues regulate EC migration and proliferation, and a critical  
307 balance between these two basic cell functions is required for multicellular sprout invasion (Fig. 6n,  
308 Supplemental Table 1).

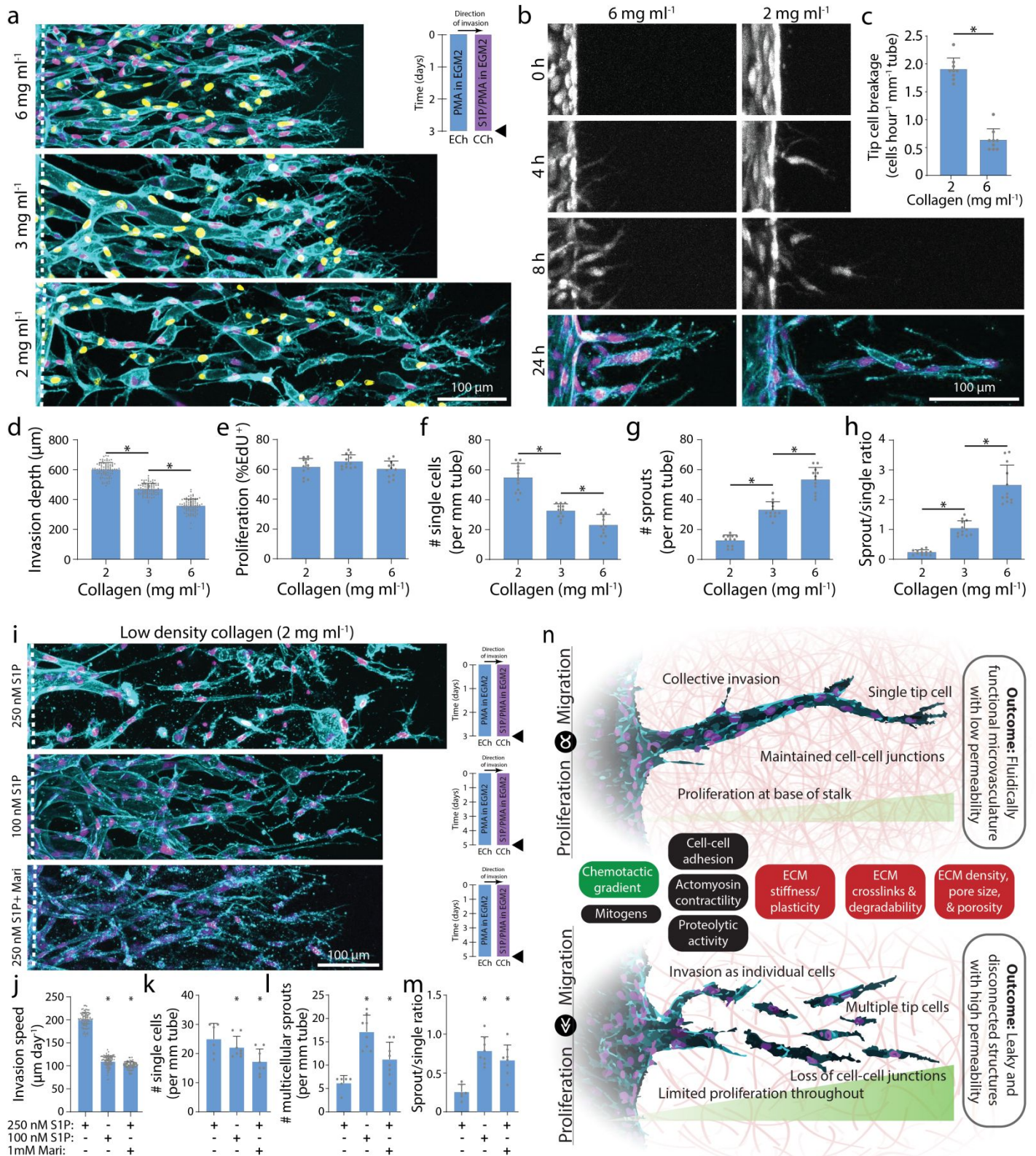


**Figure 6 | Increasing collagen density decreases invasion speed and enhances multicellular sprouting.** **a**, Representative images (max intensity projection) of invading endothelial cells in response to varying collagen density with S250:P25. UEA (cyan), nucleus (magenta), EdU (yellow). **b**, Representative time course images (max intensity projection) of invading endothelial cells (labeled with cell tracker dye) in response to varying collagen density with S250:P25. F-actin (cyan) and nucleus (magenta). **c**, Quantification of the frequency of tip cell breakage events from the parent vessel. **d-h**, Quantifications of invasion depth, proliferation, and morphology of invading endothelial cells as single cells or multicellular sprouts from conditions in (a). **i**, Representative images (max intensity projection) of invading endothelial cells in 2 mg ml<sup>-1</sup> collagen with control (S250:P25), decreased S1P (S100:P25), and MMP inhibition (S250:P25). F-

317 actin (cyan) and nucleus (magenta). **j-m**, Quantifications of invasion speed, and morphology of invading endothelial cells as single cells  
318 or multicellular sprouts. All data presented as mean  $\pm$  s.d.; \* indicates a statically significant comparison with  $P < 0.05$  (two-tailed  
319 Student's t-test (**c, j-m**) and one-way analysis of variance (**d-h**)). For tip cell breakage analysis (**c**),  $n=9$  vessel segments (each 400  $\mu\text{m}$   
320 length) per condition. For invasion depth analysis (**d**),  $n \geq 80$  vessel segments (each 100  $\mu\text{m}$  length) per condition. For proliferation and  
321 migration mode analysis (**e-h, k-m**),  $n \geq 6$  vessel segments (each 800  $\mu\text{m}$  length) per condition from  $n=2$  devices/condition (technical  
322 replicates) over  $n \geq 3$  independent studies (biological replicates). For invasion speed analysis (**j**),  $n \geq 81$  vessel segments (each 100  $\mu\text{m}$   
323 length) per condition. **n**, Schematic illustration highlighting the relationship between endothelial cell migration and proliferation on  
324 invasion morphology as multicellular sprouts (top; balanced migration and proliferation) vs single cells (bottom; excessive migration  
325 or insufficient proliferation). Soluble (green) and physical extracellular matrix (red) cues influence this balance in addition to other  
326 potential cell functions (black) that may regulate multicellular sprouting and formation of functional microvasculature.

327 **DISCUSSION**

328 EC migration and proliferation have been previously identified as key requirements for the formation of  
329 microvasculature in several models of angiogenesis<sup>33,34</sup>, but the relationship between these two fundamental  
330 cell functions has not been established. Furthermore, assessing the integrity of multicellular sprouts and  
331 resulting function of formed microvasculature has been challenging in previous *in vitro* model systems. In this  
332 work, we streamlined the fabrication of a multiplexed microfluidic device that recapitulates key aspects of 3D  
333 angiogenic sprouting and enables functional assessments of microvasculature fluidic connectivity and diffusive  
334 permeability. Tuning soluble and physical microenvironmental factors that affect EC migration and proliferation,  
335 we found that these two fundamental cell functions must be in balance to drive multicellular strand-like invasion  
336 of connected lumenized sprouts. Furthermore, microenvironmental conditions that balanced EC migration and  
337 proliferation yielded fluidically patent microvasculature with low diffusive permeability, two key traits of  
338 functional microvasculature. In stark contrast, imbalanced soluble or physical microenvironmental cues that  
339 elicited disproportionate migration and proliferation caused tip cells to break away from ensuing stalk cells; this  
340 resulted in disconnected ECs, blunt ended sprouts, fluidic leakiness, and high diffusive permeability.

341 While here we examined ECM density by tuning collagen concentration, our previous work demonstrates  
342 that ECM degradability also regulates the relationship between EC invasion speed and single vs. collective  
343 migration phenotypes, where highly degradable synthetic hydrogels increased EC invasion speed and invasion  
344 as single cells<sup>29</sup>. Of note, these synthetic matrices elicited limited EC proliferation. Coupled with the findings  
345 presented here where proliferation rates positively correlated with the diameter of lumenized neovessels,  
346 insufficient proliferation may in part explain why multicellular sprouts failed to lumenize in our previous studies  
347 employing synthetic matrices. We posit that pro-angiogenic materials must ensure multicellular invasion and  
348 also support subsequent lumenization, with proliferation potentially impacting both of these key steps of  
349 angiogenesis. As such, future investigations should aim to connect matrix structure and mechanics to EC  
350 proliferation, local density, and cytoskeletal organization during neovessel lumenization. Given the highly

351 dynamic nature of both cells and surrounding matrix during angiogenic sprouting, the use of live imaging  
352 techniques and reporters for both cell and matrix state will be essential to these endeavors<sup>22,41,42</sup>. Other cell  
353 functions that influence 3D cell migration efficiency such as proteolytic activity, cell-cell and cell-ECM adhesions,  
354 nuclear rigidity, and cytoskeletal contractility may also feed into whether cells migrate as single cells vs.  
355 collective multicellular strands<sup>29,43–46</sup> (Fig. 6n). Cell migration mode is critical in both developmental and disease  
356 processes<sup>47</sup>. Cancer cells, for example, display a diversity of migratory phenotypes during metastasis including  
357 single cells or collective strands<sup>46,48</sup>. How microenvironmental cues regulate cell invasion mode and further, how  
358 invasion mode subsequently impacts metastatic efficiency are both important unanswered questions.

359 A balance of pro- and anti-angiogenic factors normally guide physiologic angiogenesis, but in many  
360 diseases an imbalance of soluble factors can dysregulate angiogenesis<sup>8</sup>. Prior to metastasis, primary tumors  
361 stimulate rapid angiogenesis to sustain the increasing metabolic demand of the growing tumor mass<sup>49</sup>. The  
362 tumor vasculature, however, is disorganized and hyperpermeable with heterogeneous EC populations and  
363 acellular gaps along the vessel wall<sup>9,50,51</sup>. In our model system, high [S1P] drove excessively high EC invasion  
364 speeds resulting in disconnected and highly permeable microvasculature, mimicking the rapid assembly of poor  
365 quality tumor vasculature. Indeed, elevated S1P levels have previously been observed in breast cancer murine  
366 models, where paracrine signaling from breast cancer cells secreting S1P enhances tumor angiogenesis and  
367 tumor burden<sup>52,53</sup>. Hyperpermeable, tortuous vasculature impairs proper blood flow, which hampers traditional  
368 therapeutic delivery and oxygen transport. Hypoxic conditions further reduce the susceptibility of the tumor to  
369 radio- and chemotherapy<sup>54</sup>. Given recent efforts to normalize vascular phenotype to better treat solid tumors,  
370 on-a-chip models integrating cancer cells with disorganized vasculature could provide a novel testbed for anti-  
371 cancer strategies focused on rescuing tumor microvasculature phenotype and function<sup>55</sup>. Based on the findings  
372 of our work, localized delivery of EC-targeting therapeutics that dually modulate invasion and proliferation may  
373 prevent or slow the progression of angiogenesis-mediated diseases.

374 Besides excessive angiogenesis, insufficient angiogenesis also contributes to disease progression.  
375 Seemingly paradoxical, both excessive and insufficient angiogenesis occur simultaneously in distinct organs of  
376 patients suffering from diabetes mellitus<sup>10</sup>. In the retina, the onset of EC proliferation delineates the transition  
377 between low (non-proliferative) and high (proliferative) grade diabetic retinopathy where rapid angiogenesis  
378 forms hyperpermeable microvasculature that contributes to eventual blindness<sup>56</sup>. Many of these same patients  
379 also present with impaired angiogenesis in the lower extremities, which inhibits wound healing and contributes  
380 to chronic diabetic foot ulcers<sup>10</sup>. A close examination of EC proliferation and invasion during angiogenesis  
381 through the lens of altered soluble and physical microenvironmental factors in diabetic tissues could help inform  
382 new strategies to halt or promote angiogenesis in the retina or skin, respectively. Outside of diabetes, there are  
383 currently no available therapies to address insufficient angiogenesis in ischemic conditions such as critical limb  
384 and cardiac ischemia<sup>12</sup>. Towards the design of vascularized tissue transplants to treat such conditions, this work  
385 emphasizes a need for balanced EC migration and proliferation for functional angiogenesis.

386 The vascularization of large bioengineered tissue constructs at organ relevant scales remains an  
387 outstanding challenge in the tissue engineering and regenerative medicine community<sup>11</sup>. Recent advances in 3D  
388 printing technologies enable exquisite control over arteriole and venule scale microchannels in synthetic  
389 hydrogel matrices, with such constructs subsequently endothelialized by flow-through seeding<sup>57</sup>. However,  
390 current 3D bioprinting approaches cannot achieve the 5-25  $\mu\text{m}$  diameter length scale relevant to  
391 capillaries<sup>2,30,58</sup>. Furthermore, given that capillaries are narrower than fluid-suspended ECs (20-30  $\mu\text{m}$ ), flow-  
392 through seeding would prove difficult. Therefore, an integrated approach of 3D printed arteriole/venule-scale  
393 vasculature followed by controlled angiogenesis to elaborate the smallest scale capillaries may hold the most  
394 promise for generating functional hierarchical microvascular beds with potential for surgical integration<sup>59</sup>.  
395 However, a key challenge will be identifying hydrogel properties that enable high fidelity 3D printing while  
396 supporting angiogenesis, as several reports have indicated EC mechanosensitivity during migration,  
397 proliferation, and sprouting<sup>15,21,29,40,60,61</sup>. Overall, continued efforts to carefully dissect how architectural and

398 mechanical attributes of the surrounding 3D space influence angiogenesis are critical (Fig. 6n). Here, we utilized  
399 collagen hydrogels to model the collagenous stroma where angiogenesis typically occurs. However, it is  
400 challenging to orthogonally tune material properties such as stiffness, degradability, and ligand density in  
401 natural materials such as collagen<sup>62</sup>. Thus, the continued development of synthetic hydrogels and their  
402 integration with microfluidic devices will be critical to shedding deeper insight into how specific aspects of the  
403 ECM regulate angiogenesis. As many commonly utilized synthetic hydrogels lack the fibrous architecture of  
404 native tissues, recent developments in fiber-reinforced synthetic hydrogels may provide novel insights into how  
405 fibrous cues regulate EC sprouting morphology<sup>63</sup>. The information gleaned from such studies would provide rich  
406 data sets to inform computational models of angiogenic sprouting and help in identifying mechanochemical  
407 design parameters that optimize implant vascularization for regenerative tissue therapies<sup>64</sup>. A multi-disciplinary  
408 approach combining on-a-chip platforms, synthetic biomaterials, imaging of live cell molecular reporters, and  
409 computational modeling would enable prediction and control of angiogenesis across a diversity of tissue  
410 environments, essential to elucidating mechanisms of disease progression, designing therapeutics to normalize  
411 vasculature, and engineering vascularized biomaterial implants.

412 **METHODS**

413 **Reagents.** All reagents were purchased from Sigma-Aldrich and used as received, unless otherwise stated.

414 **Microfluidic device fabrication.** 3D printed moulds were designed in AutoCAD and printed via stereolithography  
415 from Protolabs (Maple Plain, MN). Polydimethylsiloxane (PDMS, 1:10 crosslinker:base ratio) devices were  
416 replica casted from 3D printed moulds, cleaned with isopropyl alcohol and ethanol, and bonded to glass  
417 coverslips with a plasma etcher. Devices were treated with 0.01% (w/v) poly-L-lysine and 0.5% (w/v) L-  
418 glutaraldehyde sequentially for 1 hour each to promote ECM attachment to the PDMS housing, thus preventing  
419 hydrogel compaction from cell-generated forces. 300  $\mu\text{m}$  stainless steel acupuncture needles (Lhasa OMS,  
420 Weymouth, MA) were inserted into each device and sterilized. Type I rat tail collagen (Corning, Corning, NY) was  
421 prepared as in Doyle<sup>65</sup>, injected into each device, and polymerized around each set of needles for 30 minutes at  
422 37°C. Collagen hydrogels were hydrated in EGM2 for 2 hours and needles were removed to form 3D hollow  
423 channels fully embedded within collagen, positioned 400  $\mu\text{m}$  away from PDMS and glass boundaries.

424 **Device cell seeding and culture.** Human umbilical vein endothelial cells (HUVEC, Lonza, Switzerland) were  
425 cultured in endothelial growth media (EGM2, Lonza). HUVECs were passaged upon achieving confluency at a  
426 1:4 ratio and used in studies from passages 4 to 9. A 20  $\mu\text{l}$  solution of suspended HUVECs was added to one  
427 reservoir of the endothelial channel and inverted for 30 minutes to allow cell attachment to the top half of the  
428 channel, followed by a second seeding with the device upright for 30 minutes to allow cell attachment to the  
429 bottom half of the channel. HUVEC solution density was varied with collagen density as attachment efficiency  
430 was dependent on collagen density (1.5 M/ml for 2  $\text{mg ml}^{-1}$ , 2 M/ml for 3  $\text{mg ml}^{-1}$  and 5 M/ml for 6  $\text{mg ml}^{-1}$ ).  
431 HUVEC seeding densities were determined experimentally to achieve parent vessels with consistent cell  
432 densities across each collagen density (Supplemental Fig. 1c). HUVECs reached confluency and self-assembled  
433 into stable parent vessels over 24 hours. Media and chemokines were refreshed every 24 hours and devices  
434 were cultured with continual reciprocating flow utilizing gravity-driven flow on a seesaw rocker plate at 0.33 Hz.

435 To inhibit cell proliferation, cells were treated with  $40 \mu\text{g ml}^{-1}$  mitomycin C for 2 hours. To inhibit S1P receptor,  
436 cells were treated with 100 nM FTY720 for 24 hours.

437 **Lentivirus production.** cDNA for pLenti CMV GFP Puro (658-5) was a gift from Eric Campeau and Paul Kaufman  
438 (Addgene plasmid #17448<sup>66</sup>). To generate lentivirus, plasmids were co-transfected with pCMV-VSVG (a gift from  
439 Bob Weinberg, Addgene plasmid #8454), pMDLg/pRRE, and pRSV-REC (gifts from Didier Trono, Addgene plasmid  
440 #12251 and #12253<sup>67,68</sup>) in 293T cells using the calcium phosphate precipitation method. Viral supernatants  
441 were collected after 48h, concentrated with PEG-it<sup>TM</sup> (System Biosciences, Palo Alto, CA) following the  
442 manufacturer's protocol, filtered through a  $0.45 \mu\text{m}$  filter (ThermoFisher Scientific Nalgene, Waltham, MA), and  
443 stored at  $-80^{\circ}\text{C}$ . Viral titer was determined by serial dilution and infection of HUVECs in the presence of  $10 \mu\text{g}$   
444  $\text{ml}^{-1}$  polybrene (Santa Cruz Biotechnology, Dallas, TX). Titers yielding maximal expression without cell death or  
445 detectable impact on cell proliferation or morphology were selected for studies.

446 **Fluorescent staining.** Samples were fixed with 4% paraformaldehyde and permeabilized with a PBS solution  
447 containing Triton X-100 (5% v/v), sucrose (10% w/v), and magnesium chloride (0.6% w/v) for 1 hour each at  
448 room temperature. AlexaFluor 488 phalloidin (Life Technologies, Carlsbad, CA) was utilized to visualize F-actin.  
449 4', 6-diamidino-2-phenylindole (DAPI,  $1 \mu\text{g ml}^{-1}$ ) was utilized to visualize cell nucleus. For proliferation studies,  
450 EdU was applied for the final 24 hours prior to fixation for each study. EdU fluorescent labelling was performed  
451 following the manufacturer's protocol (ClickIT EdU, Life Technologies). DyLight 649 labelled Ulex Europaeus  
452 Agglutinin-1 (UEA, 1:200, Vector Labs, Burlingame, CA) was utilized to visualize endothelial cell morphology in  
453 samples stained with EdU due to EdU ClickIT incompatibility with phalloidin staining. To visualize VE-cadherin,  
454 samples were sequentially blocked in bovine serum albumin (0.3% w/v), incubated with primary mouse  
455 monoclonal anti-VE-cadherin ( $200 \text{ ng ml}^{-1}$ , Santa Cruz Biotechnology), and incubated with secondary AlexaFluor  
456 647 goat anti-mouse IgG (H+L) ( $2 \mu\text{g ml}^{-1}$ , Life Technologies) each for 1 hour at room temperature. Fluorescently  
457 labelled collagen hydrogels were prepared as in Doyle<sup>65</sup>.

458 **Microscopy and image analysis.** Fluorescent images were captured on a Zeiss LSM800 confocal microscope.  
459 Parent vessel endothelial cell density and EdU proliferation was quantified by counting DAPI and EdU positive  
460 cell nuclei. Invasion depth was quantified as the distance from the parent vessel edge to the tip cell and  
461 measured in FIJI. Invasion depth measurements were performed at 100  $\mu\text{m}$  intervals along the parent vessel  
462 (Supplemental Fig. 2). Leading edge single cells were quantified as the number of single cells in the leading 150  
463  $\mu\text{m}$  front of cell invasion (Supplemental Fig. 2). Sprouts were quantified as the number of connected  
464 multicellular sprouts (parent vessel edge to tip cell) with a length greater than half the maximum invasion depth  
465 per condition (Supplemental Fig. 2). Sprout diameter measurements were performed in FIJI; diameter  
466 measurements smaller than the width of a cell nuclei (10  $\mu\text{m}$ ) were not included in the analysis to avoid  
467 measurements of smaller, non-lumenized cellular structures such as tip cell protrusions that would skew  
468 diameter measurements to lower values.

469 **Single vs. multicellular sprout analysis.** Single cell and multicellular sprout analysis was performed manually in  
470 FIJI utilizing fluorescent markers of nuclei and F-actin. This analysis was performed utilizing single z-slices within  
471 a 300  $\mu\text{m}$  z-stack. Leading edge single cells were quantified as the number of isolated single cells without actin  
472 connections to other cells in the leading 150  $\mu\text{m}$  front of cell invasion (Supplemental Fig. 2). Sprouts were  
473 quantified as the number of connected multicellular sprouts with F-actin connections from the parent vessel  
474 edge to tip cell and a length greater than half the maximum invasion depth per condition (Supplemental Fig. 2).  
475 The parent vessel edge was clearly distinguished utilizing single z-slice views (Supplemental Movies 1-5).

476 **Neovessel permeability measurement.** To assess fluidic connectivity and diffusive permeability, endothelial  
477 cells were first allowed to invade and reach the chemokine channel over 10-14 day culture. Diffusive  
478 permeability was quantified as in Polacheck et al.<sup>69</sup> Fluorescent dextran (70 kDa Texas Red, Thermo Fisher) was  
479 incorporated into EGM2 media at 12.5  $\mu\text{g ml}^{-1}$  and dextran diffusion was imaged at 1 second intervals to  
480 measure the flux of dextran from neovessels into the ECM. The resulting diffusion profile was fitted to a dynamic  
481 mass-conservation equation as in Adamson et al.<sup>70</sup> with the diffusive-permeability coefficient ( $P_D$ ) defined

482 by  $J = P_D(c_{\text{vessel}} - c_{\text{ECM}})$ , where  $J$  is the mass flux of dextran,  $c_{\text{vessel}}$  is the concentration of dextran in the vessel,  
483 and  $c_{\text{ECM}}$  is the concentration of dextran in the perivascular ECM.

484 **Statistics.** Statistical significance was determined by one-way analysis of variance (ANOVA) or two-sided  
485 student's t-test where appropriate, with significance indicated by  $p < 0.05$ . Sample size is indicated within  
486 corresponding figure legends and all data are presented as mean  $\pm$  standard deviation.

487 **Data availability.** The data that support the findings of this study are available from the corresponding author  
488 upon reasonable request.

#### 489 **Author contributions**

490 W.Y.W. and B.M.B. designed the experiments. W.Y.W, D.L., and E.H.J. conducted experiments and  
491 analyzed the data. W.J.P. performed permeability analysis. W.Y.W. and B.M.B. wrote the manuscript. All authors  
492 reviewed the manuscript.

#### 493 **Conflict of interest**

494 The authors declare no competing interests.

#### 495 **Acknowledgement**

496 This work was supported in part by the National Institutes of Health (HL124322). W.Y.W acknowledges  
497 financial support from the University of Michigan Rackham Merit Fellowship and the National Science  
498 Foundation Graduate Research Fellowship Program (DGE1256260).

499

500 **References**

- 501 1. Huxley, V. & Rumbaut, R. The Microvasculature As A Dynamic Regulator Of Volume And Solute  
502 Exchange. *Clin. Exp. Pharmacol. Physiol.* **27**, 847–854 (2000).
- 503 2. Aird, W. C. Spatial and temporal dynamics of the endothelium. *Journal of Thrombosis and Haemostasis*  
504 **3**, 1392–1406 (2005).
- 505 3. Johnson, J. M., Minson, C. T. & Kellogg, D. L. Cutaneous vasodilator and vasoconstrictor mechanisms  
506 in temperature regulation. *Compr. Physiol.* **4**, 33–89 (2014).
- 507 4. Tonnesen, M. G., Feng, X. & Clark, R. A. F. F. Angiogenesis in wound healing. *J. Investig. Dermatology*  
508 *Symp. Proc.* **5**, 40–46 (2000).
- 509 5. Fraisl, P., Mazzone, M., Schmidt, T. & Carmeliet, P. Regulation of Angiogenesis by Oxygen and  
510 Metabolism. *Dev. Cell* **16**, 167–179 (2009).
- 511 6. Wimmer, R. A. *et al.* Human blood vessel organoids as a model of diabetic vasculopathy. *Nature* **565**,  
512 505–510 (2019).
- 513 7. Carmeliet, P. Angiogenesis in life, disease and medicine. *Nature* **438**, 932–936 (2005).
- 514 8. Carmeliet, P. & Jain, R. K. Angiogenesis in cancer and other diseases. *Nature* **407**, 249–257 (2000).
- 515 9. Siemann, D. W. The unique characteristics of tumor vasculature and preclinical evidence for its selective  
516 disruption by Tumor-Vascular Disrupting Agents. *Cancer Treat. Rev.* **37**, 63–74 (2011).
- 517 10. Martin, A., Komada, M. R. & Sane, D. C. Abnormal angiogenesis in diabetes mellitus. *Med. Res. Rev.*  
518 **23**, 117–145 (2003).
- 519 11. Novosel, E. C., Kleinhans, C. & Kluger, P. J. Vascularization is the key challenge in tissue engineering.  
520 *Adv. Drug Deliv. Rev.* **63**, 300–311 (2011).
- 521 12. Losordo, D. W. & Dimmeler, S. Therapeutic angiogenesis and vasculogenesis for ischemic disease. Part  
522 II: Cell-based therapies. *Circulation* **109**, 2692–2697 (2004).
- 523 13. Francavilla, C., Maddaluno, L. & Cavallaro, U. The functional role of cell adhesion molecules in tumor  
524 angiogenesis. *Semin. Cancer Biol.* **19**, 298–309 (2009).
- 525 14. Potente, M., Gerhardt, H. & Carmeliet, P. Basic and Therapeutic Aspects of Angiogenesis. *Cell* **146**,  
526 873–887 (2011).
- 527 15. Crosby, C. O. & Zoldan, J. Mimicking the physical cues of the ECM in angiogenic biomaterials. *Regen.*  
528 *Biomater.* **6**, 61–73 (2019).
- 529 16. Nowak-Sliwinska, P. *et al.* *Consensus guidelines for the use and interpretation of angiogenesis assays.*  
530 *Angiogenesis* **21**, (Springer Netherlands, 2018).
- 531 17. Hayer, A. *et al.* Engulfed cadherin fingers are polarized junctional structures between collectively  
532 migrating endothelial cells. *Nat. Cell Biol.* **18**, (2016).
- 533 18. Baker, B. M. & Chen, C. S. Deconstructing the third dimension – how 3D culture microenvironments  
534 alter cellular cues. *J. Cell Sci.* **125**, 3015–3024 (2012).
- 535 19. Gerhardt, H. *et al.* VEGF guides angiogenic sprouting utilizing endothelial tip cell filopodia. *J. Cell Biol.*  
536 **161**, 1163–1177 (2003).
- 537 20. Jakobsson, L. *et al.* Endothelial cells dynamically compete for the tip cell position during angiogenic  
538 sprouting. *Nat. Cell Biol.* **12**, 943–953 (2010).
- 539 21. Bordeleau, F. *et al.* Matrix stiffening promotes a tumor vasculature phenotype. *Proc. Natl. Acad. Sci.*  
540 **114**, 492–497 (2017).
- 541 22. Juliar, B. A., Keating, M. T., Kong, Y. P., Botvinick, E. L. & Putnam, A. J. Sprouting angiogenesis  
542 induces significant mechanical heterogeneities and ECM stiffening across length scales in fibrin  
543 hydrogels. *Biomaterials* **162**, 99–108 (2018).
- 544 23. Ghajar, C. M., Blevins, K. S., Hughes, C. C. W., George, S. C. & Putnam, A. J. Mesenchymal stem cells  
545 enhance angiogenesis in mechanically viable prevascularized tissues via early matrix metalloproteinase  
546 upregulation. *Tissue Eng.* **12**, 2875–2888 (2006).
- 547 24. Chen, M. B. *et al.* On-chip human microvasculature assay for visualization and quantification of tumor

- 548 cell extravasation dynamics. *Nat. Protoc.* **12**, 865–880 (2017).
- 549 25. Polacheck, W. J. *et al.* A non-canonical Notch complex regulates adherens junctions and vascular barrier  
550 function. *Nature* **552**, 258–262 (2017).
- 551 26. Akbari, E., Szychalski, G. B. & Song, J. W. Microfluidic approaches to the study of angiogenesis and the  
552 microcirculation. *Microcirculation* **24**, e12363 (2017).
- 553 27. Alimperti, S. *et al.* Three-dimensional biomimetic vascular model reveals a RhoA, Rac1, and N-cadherin  
554 balance in mural cell–endothelial cell-regulated barrier function. *Proc. Natl. Acad. Sci.* **114**, 8758–8763  
555 (2017).
- 556 28. Nguyen, D.-H. T. *et al.* Biomimetic model to reconstitute angiogenic sprouting morphogenesis in vitro.  
557 *Proc. Natl. Acad. Sci. U. S. A.* **110**, 6712–7 (2013).
- 558 29. Trappmann, B. *et al.* Matrix degradability controls multicellularity of 3D cell migration. *Nat. Commun.*  
559 **8**, 371 (2017).
- 560 30. Traore, M. A. & George, S. C. Tissue Engineering the Vascular Tree. *Tissue Engineering - Part B:*  
561 *Reviews* **23**, 505–514 (2017).
- 562 31. Kinstlinger, I. S. & Miller, J. S. 3D-printed fluidic networks as vasculature for engineered tissue. *Lab on*  
563 *a Chip* **16**, 2025–2043 (2016).
- 564 32. Paik, J. H., Chae Ss, S., Lee, M. J., Thangada, S. & Hla, T. Sphingosine 1-phosphate-induced endothelial  
565 cell migration requires the expression of EDG-1 and EDG-3 receptors and Rho-dependent activation of  
566 alpha vbeta3- and beta1-containing integrins. *J. Biol. Chem.* **276**, 11830–7 (2001).
- 567 33. Ausprunk, D. H. & Folkman, J. Migration and proliferation of endothelial cells in preformed and newly  
568 formed blood vessels during tumor angiogenesis. *Microvasc. Res.* **14**, 53–65 (1977).
- 569 34. Pontes-Quero, S. *et al.* High mitogenic stimulation arrests angiogenesis. *Nat. Commun.* **10**, 2016 (2019).
- 570 35. Cross, V. L. *et al.* Dense type I collagen matrices that support cellular remodeling and microfabrication  
571 for studies of tumor angiogenesis and vasculogenesis in vitro. *Biomaterials* **31**, 8596–8607 (2010).
- 572 36. Osaki, T. *et al.* Acceleration of Vascular Sprouting from Fabricated Perfusable Vascular-Like Structures.  
573 *PLoS One* **10**, e0123735 (2015).
- 574 37. Grainger, S. J., Carrion, B., Ceccarelli, J. & Putnam, A. J. Stromal cell identity influences the in vivo  
575 functionality of engineered capillary networks formed by co-delivery of endothelial cells and stromal  
576 cells. *Tissue Eng. - Part A* **19**, 1209–1222 (2013).
- 577 38. Kosyakova, N. *et al.* Differential functional roles of fibroblasts and pericytes in the formation of tissue-  
578 engineered microvascular networks in vitro. *npj Regen. Med.* **5**, 1–12 (2020).
- 579 39. Adamson, R. H., Huxley, V. H. & Curry, F. E. Single capillary permeability to proteins having similar  
580 size but different charge. *Am. J. Physiol. Circ. Physiol.* **254**, H304–H312 (1988).
- 581 40. Ghajar, C. M. *et al.* The effect of matrix density on the regulation of 3-D capillary morphogenesis.  
582 *Biophys. J.* **94**, 1930–41 (2008).
- 583 41. Kirkpatrick, N. D., Andreou, S., Hoying, J. B. & Utzinger, U. Live imaging of collagen remodeling  
584 during angiogenesis. *Am. J. Physiol. - Hear. Circ. Physiol.* **292**, H3198–H3206 (2007).
- 585 42. Vaeyens, M. M. *et al.* Matrix deformations around angiogenic sprouts correlate to sprout dynamics and  
586 suggest pulling activity. *Angiogenesis* 1–10 (2020). doi:10.1007/s10456-020-09708-y
- 587 43. Wang, W. Y. *et al.* Extracellular matrix alignment dictates the organization of focal adhesions and directs  
588 uniaxial cell migration. *APL Bioeng.* **2**, 046107 (2018).
- 589 44. Krause, M. *et al.* Cell migration through 3D confining pores: speed accelerations by deformation and  
590 recoil of the nucleus. *Transactions B: Biological Sciences* **374**, (2018).
- 591 45. Fraley, S. I. *et al.* A distinctive role for focal adhesion proteins in three-dimensional cell motility. *Nat.*  
592 *Cell Biol.* **12**, 598–604 (2010).
- 593 46. Wang, W. Y., Davidson, C. D., Lin, D. & Baker, B. M. Actomyosin contractility-dependent matrix  
594 stretch and recoil induces rapid cell migration. *Nat. Commun.* **10**, 1186 (2019).
- 595 47. Friedl, P. & Gilmour, D. Collective cell migration in morphogenesis, regeneration and cancer. *Nat. Publ.*  
596 *Gr.* **10**, (2009).
- 597 48. Wolf, K. *et al.* Multi-step pericellular proteolysis controls the transition from individual to collective

- 598 cancer cell invasion. *Nat. Cell Biol.* **9**, 893–904 (2007).
- 599 49. Almog, N. *et al.* Transcriptional switch of dormant tumors to fast-growing angiogenic phenotype. *Cancer*  
600 *Res.* **69**, 836–844 (2009).
- 601 50. Hashizume, H. *et al.* Openings between defective endothelial cells explain tumor vessel leakiness. *Am. J.*  
602 *Pathol.* **156**, 1363–1380 (2000).
- 603 51. Di Tomaso, E. *et al.* Mosaic tumor vessels: Cellular basis and ultrastructure of focal regions lacking  
604 endothelial cell markers. *Cancer Res.* **65**, 5740–5749 (2005).
- 605 52. Nagahashi, M. *et al.* Sphingosine-1-phosphate produced by sphingosine kinase 1 promotes breast cancer  
606 progression by stimulating angiogenesis and lymphangiogenesis. *Cancer Res.* **72**, 726–735 (2012).
- 607 53. Takabe, K. *et al.* Estradiol induces export of sphingosine 1-phosphate from breast cancer cells via  
608 ABCG1 and ABCG2. (2010). doi:10.1074/jbc.M109.064162
- 609 54. Declerck, K. & Elble, R. C. *The role of hypoxia and acidosis in promoting metastasis and resistance to*  
610 *chemotherapy. Frontiers in Bioscience* **15**, (2010).
- 611 55. Jain, R. K. Normalization of tumor vasculature: an emerging concept in antiangiogenic therapy. *Science*  
612 *(80- )*. **307**, 58–62 (2005).
- 613 56. Durham, J. T. & Herman, I. M. Microvascular modifications in diabetic retinopathy. *Current Diabetes*  
614 *Reports* **11**, 253–264 (2011).
- 615 57. Grigoryan, B. *et al.* Multivascular networks and functional intravascular topologies within biocompatible  
616 hydrogels. *Science* **364**, 458–464 (2019).
- 617 58. Gong, H., Beauchamp, M., Perry, S., Woolley, A. T. & Nordin, G. P. Optical approach to resin  
618 formulation for 3D printed microfluidics. *RSC Adv.* **5**, 106621–106632 (2015).
- 619 59. Mirabella, T. *et al.* 3D-printed vascular networks direct therapeutic angiogenesis in ischaemia. *Nat.*  
620 *Biomed. Eng.* **1**, 0083 (2017).
- 621 60. Davidson, C. D., Wang, W. Y., Zaimi, I., Jayco, D. K. P. & Baker, B. M. Cell force-mediated matrix  
622 reorganization underlies multicellular network assembly. *Sci. Rep.* **9**, 12 (2019).
- 623 61. Juliar, B. A. *et al.* Cell-mediated matrix stiffening accompanies capillary morphogenesis in ultra-soft  
624 amorphous hydrogels. *Biomaterials* **230**, 119634 (2020).
- 625 62. Li, L., Eyckmans, J. & Chen, C. S. Designer biomaterials for mechanobiology. *Nat. Mater.* **16**, 1164–  
626 1168 (2017).
- 627 63. Matera, D. L., Wang, W. Y., Smith, M. R., Shikanov, A. & Baker, B. M. Fiber Density Modulates Cell  
628 Spreading in 3D Interstitial Matrix Mimetics. *ACS Biomater. Sci. Eng.* **5**, 2965–2975 (2019).
- 629 64. Heck, T. A. M., Vaeyens, M. M. & Van Oosterwyck, H. Computational Models of Sprouting  
630 Angiogenesis and Cell Migration: Towards Multiscale Mechanochemical Models of Angiogenesis. *Math.*  
631 *Model. Nat. Phenom.* **10**, 108–141 (2015).
- 632 65. Doyle, A. D. Generation of 3D collagen gels with controlled diverse architectures. *Curr. Protoc. Cell*  
633 *Biol.* **2016**, 10.20.1–10.20.16 (2016).
- 634 66. Campeau, E. *et al.* A versatile viral system for expression and depletion of proteins in mammalian cells.  
635 *PLoS One* **4**, (2009).
- 636 67. Stewart, S. A. *et al.* Lentivirus-delivered stable gene silencing by RNAi in primary cells Lentivirus-  
637 delivered stable gene silencing by RNAi in primary cells. *Rna* **9**, 493–501 (2003).
- 638 68. Dull, T. *et al.* A third-generation lentivirus vector with a conditional packaging system. *J. Virol.* **72**,  
639 8463–71 (1998).
- 640 69. Polacheck, W. J., Kutys, M. L., Tefft, J. B. & Chen, C. S. Microfabricated blood vessels for modeling the  
641 vascular transport barrier. *Nat. Protoc.* **14**, 1425–1454 (2019).
- 642 70. Adamson, R. H., Lenz, J. F. & Curry, F. E. Quantitative Laser Scanning Confocal Microscopy on Single  
643 Capillaries: Permeability Measurement. *Microcirculation* **1**, 251–265 (1994).
- 644

645 ***Author contributions***

646 W.Y.W. and B.M.B. designed the experiments. W.Y.W, D.L., and E.H.J. conducted experiments and  
647 analyzed the data. W.J.P. performed permeability analysis. W.Y.W. and B.M.B. wrote the manuscript. All authors  
648 reviewed the manuscript.

649 ***Conflict of interest***

650 The authors declare no competing interests.

651 ***Acknowledgement***

652 This work was supported in part by the National Institutes of Health (HL124322). W.Y.W acknowledges  
653 financial support from the University of Michigan Rackham Merit Fellowship and the National Science  
654 Foundation Graduate Research Fellowship Program (DGE1256260).

